

# Stochastic Phase Segregation on Surfaces

Prerna Gera and David Salac\*

*Department of Mechanical and Aerospace Engineering,*

*University at Buffalo, Buffalo, New York 14260-4400*

(Dated: April 19, 2017)

## Abstract

Phase separation and coarsening is a phenomenon commonly seen in binary physical and chemical systems that occur in nature. Often times, thermal fluctuations, modeled as stochastic noise, are present in the system and the phase segregation process occurs on a surface. In this work, the segregation process is modeled via the Cahn-Hilliard-Cook model, which is a fourth-order parabolic stochastic system. Coarsening is analyzed on two sample surfaces: a unit sphere and a dumbbell using a variety and a statistical analysis of the growth rate is performed. The influence of noise level and mobility is also investigated. It is also shown that a log-normal distribution fits the results well.

---

\*Corresponding author: [davidsal@buffalo.edu](mailto:davidsal@buffalo.edu)

## I. INTRODUCTION

Domains on curved surfaces are found in numerous industrial and biomedical applications such as chemical reactors [1], enhanced oil recovery [2], and pulmonary functions [3]. These domains have the potential to change the dynamics of these system significantly. For example, surfactants on bubbles or droplets can reduce the velocity of the rising bubble [4] or they can prevent the coalescence of multiple bubbles [1]. The effect of surface molecules can also be seen in the area of biology such as the cell membrane [5]. The cell membrane is composed of multiple components including saturated lipids, unsaturated lipids and cholesterol. The saturated lipid molecules combine with the cholesterol to form lipid domains, with these lipid domains being more ordered and stable than the surrounding membrane [6]. Due to the nature of the domains, experimental visualization is difficult with artifacts and errors influencing the accuracy of the experimental results. Using numerical tools and mathematical modeling to investigate the dynamics of surface domains can provide important information not obtainable experimentally. In addition to biological membranes, other interesting phase dynamics on a curved surface includes crystal growth [7], phase separation within thin films [8], and phase separation patterns in diblock polymers [9]. With this motivation, the goal of this work is to study the phase segregation dynamics on a smooth curved surface.

The Cahn-Hilliard (CH) equation is a popular model to capture and investigate phase segregation dynamics in a multi-component system. It describes the temporal evolution of an order parameter that defines the phase or domain, with the driving force given by energy minimization under the assumption of quantity conservation. Pioneered by Cahn & Hilliard in 1958 [10], the equation has been used to model many physical systems including binary alloys [10], polymers and ceramics [11], droplet breakup [12], liquid-liquid jets pinching off [13], multicomponent lipid vesicles [14], and for the tracking of tumor growth [15].

In 1970 Cook proposed to make the system more realistic by including internal thermal fluctuations, which are represented by a conserved noise source term. This extension is more commonly known as the Cahn-Hilliard-Cook (CHC) model [16]. The first numerical work to study the CHC equation was done by Langer [17]. This work was compared against theoretical results and it was concluded that the thermal fluctuations play an important role in the early stage of phase dynamics [17]. To understand the early stages better, Grant et al. developed a perturbation theory for a long range force limit and utilized numerical methods

to investigate the model [18]. Rodgers et al. studied convergence of the solution, the growth characteristics of the domain formation and the effect of noise [19]. The impact of noise in the CHC has also been analyzed by several other works, see Refs. [20–22] for examples. Using this model, the influence of non-equilibrium lipid transport on a membrane [23], dendritic branching [24], nucleation in micro-structures [25], and the dynamics of solvent based organic cells [26], have also been investigated.

The Cahn-Hilliard-Cook model can be solved computationally using a variety of numerical methods including finite differences [27–29], finite elements [30–32], and spectral methods [33, 34]. Most investigations using the CHC model are two-dimensional, although there are several which investigate three-dimensional systems [22]. In this work a method to model the Cahn-Hilliard-Cook system on an arbitrary two-dimensional surface in three-dimensional space is presented. Prior works in modeling the phase-segregation on curved surfaces have been performed at the nanometer level, including those based on Molecular Dynamics (MD) [35–37], where atomistic level forces can be incorporated. A limit of these MD simulations is the length and time scales which can be investigated. To allow for longer time-scales and larger domain sizes to be investigated, coarse grained methods such as Dissipative Particle Dynamics (DPD) have been used [38]. An alternate technique is to examine phase segregation on surfaces using a continuum-based method, which is the approach taken here. Samples of this type of work in the absence of noise have been presented in the past [14, 39–41].

The work here is based on a splitting method previously used to model the Cahn-Hilliard equation [42, 43]. The coarsening rates for the CH and CHC systems are compared using both constant and variable mobility, in addition to varying noise levels. While in an actual system thermal fluctuations may also influence the shape of the underlying interface, this is not considered here.

In the following section of the paper the governing equations of the system is described. The numerical tools and techniques that are used and the overall algorithm is then explained. Phase segregation on a sphere is examined and systematically investigated. A statistical analysis on growth rate of the domains that appear on the sphere is done. Further, the effect of the underlying geometry is also shown as the statistical analysis of the growth rate on a dumbbell is presented.

## II. MATHEMATICAL FORMULATION

In this work, the dynamics of phase separation and coarsening of a two-component system on a surface is described by the Cahn-Hilliard equation. This equation captures how a system will change over time to reduce the overall free energy of a multicomponent system. Further, the segregation process is restricted to a co-dimension one interface and thus will involve surface derivatives. Let  $\Gamma(\mathbf{x}, t)$  define the interface at any point in time. The concentration field  $f(\mathbf{x}, t)$  is defined on  $\Gamma(\mathbf{x}, t)$  such that  $0 \leq f(\mathbf{x}, t) \leq 1$  is the concentration of one surface phase while the concentration of the remaining surface phase is  $1 - f(\mathbf{x}, t)$ . Using this, the CH equation is derived from the mass-continuity equation,

$$\frac{\partial f}{\partial t} + \nabla_s \cdot \mathbf{J}_s = 0, \quad (1)$$

where  $\mathbf{J}_s$  is the surface flux and  $\nabla_s \cdot$  is the surface divergence while  $\nabla_s = \mathbf{P} \nabla$  is the surface gradient [44] and  $\mathbf{P} = \mathbf{I} - \mathbf{n} \otimes \mathbf{n}$  is the Laplace-Beltrami operator for an outward pointing unit normal to the interface  $\mathbf{n}$ . Using Fick's law the surface flux is related to the chemical potential  $\mu$  via the surface gradient and a mobility  $\nu(f)$  [43],

$$\mathbf{J}_s = -\nu(f) \nabla_s \mu. \quad (2)$$

From these two equations,

$$\frac{\partial f}{\partial t} - \nabla_s \cdot (\nu(f) \nabla_s \mu) = 0. \quad (3)$$

Two types of mobility are considered in this work. The first type is constant mobility,

$$\nu(f) = \nu_0, \quad (4)$$

where  $\nu_0$  is the surface mobility constant. This type of mobility is appropriate when molecules can freely move through bulk phases. The second type is more appropriate for situations where the majority of molecular motion occurs at the interface between phases. In this case a degenerate mobility is defined as

$$\nu(f) = 4\nu_0 f(1 - f). \quad (5)$$

It should be noted that for the variable mobility case, the overall mobility in the bulk is very small, which is often the case in realistic system [45, 46]. It is also possible to utilize other mobilities, as has been recently investigated [47].



The chemical potential  $\mu$  can be derived by applying the variational derivative to the free energy of the surface phase field [48]. Intuitively, it is expected that the local free energy will depend on the homogeneous free energy and the energy due to the interface separating the phases [10]. This energy functional can thus be written as,

$$E[f] = \int_{\Gamma(\mathbf{x},t)} \left( g(f) + \frac{\epsilon^2}{2} (\nabla_s f)^2 \right) dA. \quad (6)$$

The first term is the free energy of the homogeneous solution, while the second term is the interfacial energy, defined using the surface gradient of the concentration field, where  $\epsilon$  is a constant associated with the domain interface energy. This form of energy functional is also known as the Landau-Ginzberg free energy functional [41]. Taking the variational derivative of the free energy functional with respect to a change in the concentration variable results in the chemical potential field [30, 49],

$$\mu = g'(f) - \epsilon^2 \Delta_s f, \quad (7)$$

where  $\Delta_s = \nabla_s \cdot \nabla_s$  is the surface Laplacian and  $g'(f)$  is the derivative of the mixing energy with respect to argument  $f$ .

The homogeneous free energy is usually described using a double well potential. In this work a simple mixing energy of

$$g(f) = f^2(1 - f)^2, \quad (8)$$

as shown in Fig 1, is used. The points  $f_1$  and  $f_2$  are called the spinodes, and are defined by  $\partial^2 g / \partial^2 f = 0$ . The region between by  $f_1$  and  $f_2$ , given by  $\partial^2 g / \partial^2 f < 0$ , is known as the spinodal region, where a single phase decomposes into two phases. In this simple mixing energy the equilibrium concentration of the two phases are defined by the two wells at concentrations  $f = 0$  and  $f = 1$ .

To define the Cahn-Hilliard-Cook equation, a white Gaussian noise [19, 23] is added to the deterministic Cahn-Hilliard equation,

$$\frac{\partial f(\mathbf{x}, t)}{\partial t} = \nabla_s \cdot (\nu \nabla_s \mu) + \xi(\mathbf{x}, t) \quad (9)$$

where  $\xi$  denotes a stochastic Gaussian white noise dictated by the Fluctuation Dissipation Theorem with mean  $\langle \xi \rangle = 0$  and variance  $\langle \xi(\mathbf{x}, t), \xi(\mathbf{x}', t') \rangle = -2\nu k_B T \delta(t - t') \Delta_s \delta(\mathbf{x} - \mathbf{x}')$ , where  $\delta$  is the Dirac delta function [22, 23]. The Fluctuation Dissipation Theorem implies

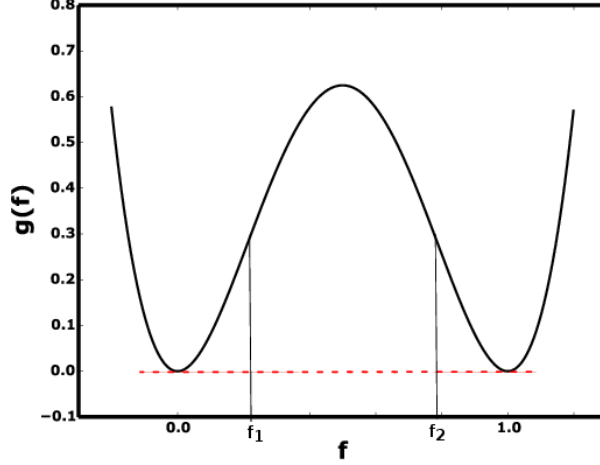


FIG. 1: Homogeneous free energy of mixing

that the random noise that is added is uncorrelated in time but partially correlated, specifically conserved, in space. The Laplacian in front of the Dirac delta function appears as this Langevin force term is present in a system that is characterized by conserved fields. These kinds of stochastic fluctuating partial differential equations are currently under investigation [50].

### A. Non-Dimensional System

The dimensionless CHC equation that governs the evolution of domains is

$$\frac{\partial f}{\partial \hat{t}} = \frac{1}{\text{Pe}} \hat{\nabla}_s \cdot \left( \hat{\nu} \hat{\nabla}_s \hat{\mu} \right) + \hat{\xi}, \quad (10)$$

where the dimensionless units are represented by  $(\hat{\cdot})$  and Pe is the surface Peclet number, which relates the strength of any surface advection to diffusion. The dimensionless parameters are defined as follows.

$$\begin{aligned} \hat{t} &= \frac{t}{t_0}, \quad \hat{\nu} = \frac{\nu}{\nu_0}, \quad \hat{\mu} = \frac{\mu}{\mu_0}, \\ \hat{\nabla}_s &= l_0 \nabla_s, \\ \text{Pe} &= \frac{l_0^2}{t_0 \mu_0 \nu_0}, \quad \text{Cn}^2 = \frac{\epsilon^2}{\mu l_0^2} \\ \langle \hat{\xi}(\mathbf{x}, t), \hat{\xi}(\mathbf{x}', t') \rangle &= -\sigma \hat{\nu} \delta(t - t') \hat{\Delta}_s^2 \delta(\mathbf{x} - \mathbf{x}'), \end{aligned} \quad (11)$$

where  $l_0$  is the characteristic length,  $t_0$  is the characteristic time,  $\mu_0$  is characteristic chemical potential,  $\nu_0$  is characteristic mobility,  $\text{Cn}^2$ , relates the ratio of the domain interface energy

to the chemical potential where  $Cn$  is called the Cahn number, and  $\sigma$  is the noise intensity defined as  $\sigma = (2k_B T / \mu_0)^2$ . Using this notation the dimensionless mobility is now  $\hat{\nu} = 1$  for the constant mobility case and  $\hat{\nu} = 4f(1 - f)$  for the variable mobility case. The dimensionless chemical potential equation is,

$$\hat{\mu} = \frac{\partial \hat{g}}{\partial f} - Cn^2 \hat{\Delta}_s f. \quad (12)$$

Using Eq. (10) and Eq. (12), and dropping the  $(\hat{\cdot})$  notation the following fourth-order evolution equation for  $f(\mathbf{x}, t)$  is obtained:

$$\frac{\partial f}{\partial t} + \frac{Cn^2}{Pe} \nabla_s \cdot (\nu \nabla_s \Delta_s f) = \frac{1}{Pe} \nabla_s \cdot (\nu \nabla_s g'(f)) + \xi. \quad (13)$$

### III. NUMERICAL METHOD

In this section we discuss the numerical methods used to model phase dynamics on a curved surface. The interface is described using a level set Jet method [51, 52]. To solve the surface evolution equation, we use the Closest Point Method, which is described in section III B. We discretize the system using second-order, centered finite differencing techniques while a semi-implicit time discretization is employed.

#### A. Defining the Curved Surface Using Level-Sets

The level-set method is a tool to define and track an interface. Introduced by Osher and Sethian [53], this method has been used in a variety of applications including medical imaging [54], crystal growth [55], crack patterns [56], and semiconductor processing [57]. The idea is to define the interface implicitly through the use of an auxiliary mathematical function, akin to density, which allows for complex motion and topological changes such as merging and pinching. For details, readers can refer to Osher and Fedkiw [58] or Sethian and Smereka [59].

Let  $\Gamma(\mathbf{x}, t)$  be the interface separating regions  $\Omega^-$  and  $\Omega^+$ . This interface is represented by the zero set of a higher dimensional level-set function  $\phi(\mathbf{x}, t)$ ,

$$\Gamma(\mathbf{x}, t) = \{\mathbf{x} : \phi(\mathbf{x}, t) = 0\}, \quad (14)$$

see Fig. 2. The region  $\Omega^-$  is given by  $\phi(\mathbf{x}, t) < 0$  while  $\Omega^+$  is defined as the region occupying  $\phi(\mathbf{x}, t) > 0$ .

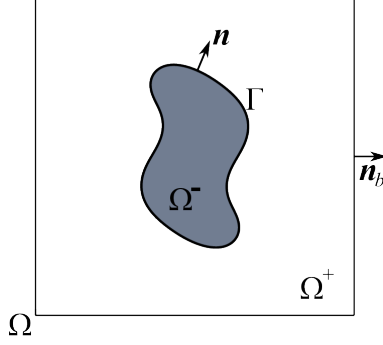


FIG. 2: The computational domain.

A significant advantage of this implicit representation is that many geometric quantities can easily be computed. For example, the normal and total curvature (sum of the principle curvatures) of the interface can be defined as,

$$\mathbf{n} = \frac{\nabla\phi}{\|\nabla\phi\|}, \quad H = \nabla \cdot \frac{\nabla\phi}{\|\nabla\phi\|}. \quad (15)$$

To model a surface differential equation accurate information must exist about the location of the interface. As the interface will, in general, not coincide with grid points interpolation schemes must be used to determine the location of the interface. To aid in this, an extension of the base level set method is used. The idea is to track not only a single level set function  $\phi$ , but also derivatives of the level set. A grouping of this information has been called a “jet” of information [51]. Using this jet, it is possible to define high-order interpolants without the need for derivative approximations. For example, using a jet which consists of the level set function,  $\phi$ , in addition to gradient vector field,  $\phi_x$  and  $\phi_y$ , and the first cross-derivative,  $\phi_{xy}$ , it would be possible to define a cubic Hermite interpolant on a two-dimensional Cartesian grid without the need for derivative approximations. Additional information about the Jet level-set method can be found in the work of Seibold, Rosales, and Nave [51].

## B. Phase Field Solver

The Cahn-Hilliard-Cook system, Eq. (13), can be written as a pair of coupled, second-order differential equations [42, 43],

$$\frac{\partial f}{\partial t} - \frac{1}{\text{Pe}} \nabla_s \cdot (\nu \nabla_s \mu) - \xi = 0 \quad \text{and} \quad \mu + \text{Cn}^2 \Delta_s f = g'(f). \quad (16)$$

Here, a second-order backward-finite-difference (BDF2) scheme [60] is used to discretize in time. The system can then be written as

$$\begin{bmatrix} \mathbf{I} & \text{Cn}^2 \mathbf{L}_s \\ -\frac{2\Delta t}{3\text{Pe}} \mathbf{L}_s^\nu & \mathbf{I} \end{bmatrix} \begin{bmatrix} \boldsymbol{\mu}^{n+1} \\ \mathbf{f}^{n+1} \end{bmatrix} = \begin{bmatrix} g'(\hat{\mathbf{f}}) \\ \frac{4}{3}\mathbf{f}^n - \frac{1}{3}\mathbf{f}^{n-1} + \frac{2}{3}\Delta t \xi^n \end{bmatrix}, \quad (17)$$

where  $\Delta t$  is a fixed time step. In the above block system  $\mathbf{I}$  is the identity matrix, the constant-coefficient surface Laplacian is given by  $\mathbf{L}_s \approx \Delta_s$ , and the variable-coefficient surface Laplacian is given by  $\mathbf{L}_s^\nu \approx \nabla_s \cdot (\nu \nabla_s)$ . The solutions  $\mathbf{f}^n$  and  $\mathbf{f}^{n-1}$  are at times  $t^n$  and  $t^{n-1}$ , respectively, and the approximation to the solution at time  $t^{n+1}$  is given by  $\hat{\mathbf{f}} = 2\mathbf{f}^n - \mathbf{f}^{n-1}$ .

As this is a surface partial differential equation, specialized methods are required to evolve it properly. In this work the Closest Point Method is used. The Closest Point Method was first developed and analyzed by Ruuth and Merriman [61] and has been modified to increase numerical stability and accuracy [62]. The basic idea is to extend the solution to a surface differential equation away from the interface such that it is constant in the normal direction. With this extension, it is possible to write a surface differential equation as a standard differential equation in the embedding space. It has been previously shown that the surface Laplacian operator can be computed with second order accuracy using linear and cubic polynomial interpolations[63].

Let  $\mathbf{E}_1$  be a linear polynomial interpolation operator and  $\mathbf{E}_3$  be a cubic polynomial interpolation operator. For any point  $\mathbf{x}$  not on the interface these operators return the value of a function at the interface point closest to  $\mathbf{x}$ . For example, the operation  $\mathbf{E}_3 \mathbf{f}$  returns the value of  $f$  at the point on the interface closest to  $\mathbf{x}$  using the cubic interpolation function. Using this notation, the block matrix in Eq. (17) is re-written as

$$\begin{bmatrix} \mathbf{I} & \text{Cn}^2 [\mathbf{E}_1 \mathbf{L} + \alpha (\mathbf{E}_3 - \mathbf{I})] \\ -\frac{2\Delta t}{3\text{Pe}} [\mathbf{E}_1 \mathbf{L}^\nu + \alpha (\mathbf{E}_3 - \mathbf{I})] & \mathbf{I} \end{bmatrix} \begin{bmatrix} \boldsymbol{\mu}^{n+1} \\ \mathbf{f}^{n+1} \end{bmatrix} = \begin{bmatrix} g'(\hat{\mathbf{f}}) \\ \frac{4}{3}\mathbf{f}^n - \frac{1}{3}\mathbf{f}^{n-1} + \frac{2}{3}\Delta t \tilde{\xi}^n \end{bmatrix}, \quad (18)$$

with  $\alpha = 6/h^2$  where  $h$  is the uniform grid spacing and  $\mathbf{L} \approx \Delta$  represents the Cartesian finite difference approximation to the constant standard Laplacian and  $\mathbf{L}^\nu \approx \nabla \cdot (\tilde{\nu} \nabla)$  represents the Cartesian finite difference approximation to the variable-coefficient Laplacian.

Quantities denoted with  $(\sim)$  indicate that the value has been extended off the interface. The addition of the  $\alpha$  term, also known as a side condition, ensures that the solutions are constant in the normal direction. If this extension holds then surface operators can be replaced with standard Cartesian operators. See Chen and Macdonald for complete details [63].

The block system shown in Eq. (18) is solved using the preconditioned Flexible GMRES algorithm available in PETSc [64–66]. The preconditioner is based on an incomplete Schur complement. Let  $\mathbf{L}_E = \mathbf{E}_1 \mathbf{L} + \alpha (\mathbf{E}_3 - \mathbf{I})$  and  $\mathbf{L}_E^\nu = \mathbf{E}_1 \mathbf{L}^\nu + \alpha (\mathbf{E}_3 - \mathbf{I})$ . The preconditioner is then

$$\mathbf{P} = \begin{bmatrix} \mathbf{I} & -\text{Cn}^2 \mathbf{L}_E \\ 0 & \mathbf{I} \end{bmatrix} \begin{bmatrix} \mathbf{I} & 0 \\ 0 & \hat{\mathbf{S}}^{-1} \end{bmatrix} \begin{bmatrix} \mathbf{I} & 0 \\ \frac{2\Delta t}{3\text{Pe}} \mathbf{L}_E^\nu & \mathbf{I} \end{bmatrix}. \quad (19)$$

The Schur complement is written as  $\mathbf{S} = \mathbf{I} + \frac{2\text{Cn}^2 \Delta t}{3\text{Pe}} \mathbf{L}_E \mathbf{L}_E^\nu$ . The application of the approximate Schur complement inverse,  $\hat{\mathbf{S}}^{-1}$ , is obtained via 5 iterations of an algebraic multigrid preconditioning method [67].

### C. Noise Calculation

The noise term is calculated based on the Fluctuation Dissipation Theorem as follows,

$$\xi(\mathbf{x}, t) = \mathcal{N}(0, -\sigma\nu\delta(t - t')\Delta_s\delta(\mathbf{x} - \mathbf{x}')). \quad (20)$$

Writing the mean and the variance in discrete form,

$$\langle \xi_{\mathbf{x}_\Gamma}^n \rangle = 0, \quad (21)$$

$$\langle \xi_{\mathbf{x}_\Gamma}^n \xi_{\mathbf{y}_\Gamma}^{n+1} \rangle = -\sigma\nu(f_{\mathbf{x}_\Gamma}^n) \frac{\delta_{(n)(n+1)}}{|t^n - t^{n+1}|} \Delta_s^h \frac{\delta_{(\mathbf{x}_\Gamma)(\mathbf{y}_\Gamma)}}{h^2}, \quad (22)$$

where  $\mathbf{x}_\Gamma$  and  $\mathbf{y}_\Gamma$  are two different points on the interface and  $n$  defines the time step [22]. As we are considering a two-dimensional surface, the grid size  $h$  is raised to the second power [25]. The proof of the discretization in the above can be found in reference [68].

To compute the random forcing term,  $\tilde{\xi}$ , the following procedure is used. To ensure consistency of the scheme this forcing term must be constant in the normal direction. This can be accomplished by computing the random force contribution at the closest point of any grid point and extending this quantity outwards. At a closest point, a random tangential vector is determined by choosing two random numbers,  $\rho_1$  and  $\rho_2$ , from a Gaussian distribution with zero mean and unit variance. A random surface vector is then determined by  $\boldsymbol{\rho} = \rho_1 \mathbf{t} + \rho_2 \mathbf{b}$ ,

where  $\mathbf{t}$  and  $\mathbf{b}$  are two orthonormal vectors on the surface, such as the principle directions. Once these tangential random vectors are calculated in a region around the interface, it is possible to define the random force through

$$\tilde{\xi} = \sqrt{\frac{\sigma\nu(f)}{h^2\Delta t}} \nabla_s \cdot \tilde{\boldsymbol{\rho}}, \quad (23)$$

where a constant time step,  $\Delta t$ , is assumed. Note that as the surface Laplacian is approximated numerically, it may fail to preserve the fluctuation dissipation balance in the exact sense.

#### D. Conservation of Surface Phase Concentration

After solving the system of the partial differential equation, Eq. (17), there will be certain amount of loss of surface phase concentration due to numerical diffusion. The accumulative effect may have a drastic change on the average surface concentration over time. There have been numerous attempts to fix this issue in the past, see Refs. [69–71] for examples. In this work a correction method is implemented. This method was introduced by Xu et al [72], with the idea of adjusting the surface phase concentration at the end of every time step to ensure mass conservation. Let  $f_h$ ,  $\phi$ , and  $\Gamma$  be the solution of the discrete surface phase concentration equation Eq. (18), level set and interface at a given point in time, and let  $f_0$ ,  $\phi_0$ , and  $\Gamma_0$  be the initial phase concentration, initial level set function and initial interface, respectively. Then a surface phase concentration conservation parameter,  $\beta$ , is chosen such that the following condition is true,

$$\int_{\Gamma} \beta f_h dA = \int_{\Gamma_0} f_0 dA. \quad (24)$$

Hence,  $\beta$  is computed as

$$\beta = \frac{\int_{\Gamma_0} f_0 dA}{\int_{\Gamma} f_h dA} = \frac{\int_{\Omega} f_0 \delta(\phi_0) dV}{\int_{\Omega} f_h \delta(\phi) dV} \quad (25)$$

where  $\delta$  is the Dirac delta function and the integrals are now performed over the embedding domain. The surface phase concentration is then modified at each time step as  $f = \beta f_h$ . For further details, we refer the reader to Xu et al [72].

## IV. RESULTS ON A SPHERE

In this section qualitative and quantitative results are presented using the method described in previous sections. In this section the surface will be a unit sphere. First, the sample evolution of phase dynamics is examined. Following that, a quantitative analysis on the domain dynamics is performed. This includes a convergence study to justify the grid size and time step used for the analysis. The growth rate of the domains is examined, and in particular the impact of variable and constant mobility in the system is considered. Finally, the role of noise in the system is investigated.

For simplicity, the shape considered is a unit sphere in a computational domain spanning  $[-1.25, 1.25]^3$ . Unless otherwise stated, the average concentration is set to 0.3, with an initial random perturbation of 0.01. The Peclet number is set to  $Pe = 1.0$ , the Cahn number is  $Cn = 0.015$ , and when noise is present, has intensity of  $\sigma = 10^{-5}$ . See Fig. 3 for a sample evolution.

Surface dynamics will be quantified by a characteristic length,  $\bar{R}(t)$ , for the domains present on the surface. This surface characteristic length is defined as

$$\bar{R}(t) = \frac{A(t)}{L(t)}, \quad (26)$$

where  $A(t) = \int_{\Gamma} f \, dA$  is the total area of the domains and  $L(t) = \int_{\Gamma} \|\nabla_s f\| \, dA$  is the corresponding total interface length of the domains.

### A. Sample Evolution of Phase Dynamics

In this section, the dynamics on a smooth spherical surface is examined for four cases: a) Cahn-Hilliard with constant mobility, b) Cahn-Hilliard with variable mobility, c) Cahn-Hilliard-Cook with constant mobility, d) and Cahn-Hilliard-Cook with variable mobility. In all four cases, the initial condition is a random perturbation with a magnitude of 0.01 about the average concentration of 0.3. There are three expected regimes. Initially, very rapid phase segregation will occur and a large number of domains will appear. This will be followed by slow coarsening of the domains, which results in an increasing average domain size. The final regime will be characterized by a very slow coarsening process. In the simulations performed in this work, approximately 400 domains are seen during the initial



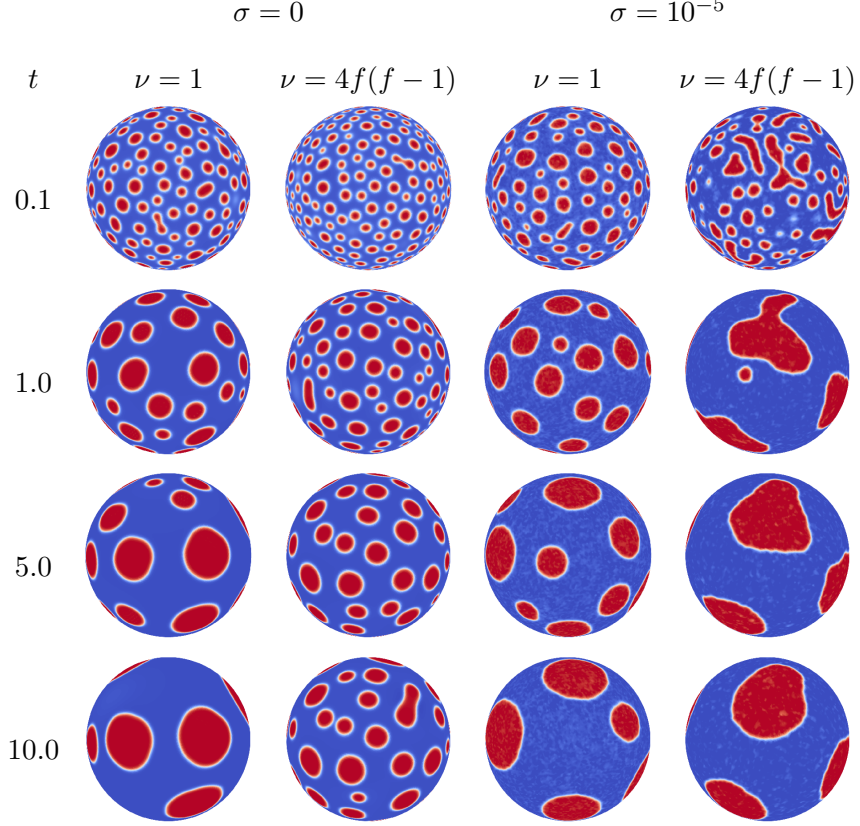


FIG. 3: Evolution for Cahn-Hilliard ( $\sigma = 0$ ) and Cahn-Hilliard-Cook ( $\sigma = 10^{-5}$ ) model with constant and variable mobility.

phase segregation process. These domains coarsen in time, and only 5 to 6 domains remain in the final slow coarsening stage. See Fig. (10) for a sample evolution.

For the case of the Cahn-Hilliard model with constant mobility, the fast phase segregation occurs up to a time of  $t = 0.1$ , see Fig. 3, thereafter the domains start to slowly coarsen in time. The primary means of coarsening in this case is spinodal decomposition, where a domain large in size grows at the expense of smaller, nearby, domains. In this type of behavior the center of each domain remains relatively fixed. The use of degenerate mobility decreases this coarsening rate but does not change the coarsening mechanism, which can be seen by comparing the first two columns of Fig. 3.

The combination of CHC and variable mobility has the effect of increasing the coarsening rate. This can be observed by visually comparing the sizes of the domains at a time of  $t = 1$ , as the general size of the domains in the CHC plus variable mobility are larger than the other three cases. This behavior will be further explored in subsequent sections.

## B. Convergence Study

The numerical convergence of the Cahn-Hilliard system in the absence of noise has been previously investigated by the authors [73]. In this section a qualitative convergence study is performed with regard to the change of the characteristic length over time. Sample plots of the characteristic length over time for both the constant and variable mobility case are shown in Fig. 4. Here four different grid sizes are considered:  $N = 97$ ,  $N = 129$ ,  $N = 161$ , and  $N = 193$ . For each case the time step is set to  $\Delta t = 5.12 \times 10^{-3}h$ , where  $h = 2.5/(N-1)$  is the grid spacing.

Initially there is a rapid decrease in the characteristic length as the system undergoes rapid phase segregation from a well-mixed interface to one with many, small domains. After this point the domains coarsen at a given rate, before reaching the near-equilibrium configuration. This middle region, after initial coarsening and before the near-equilibrium dynamics, is the region of interest.

For the constant mobility case, Fig. 4(a), the growth in this middle region, from approximately  $t = 0.1$  to  $t = 10$ , the rate is similar across all grid spacings. With variable mobility, Fig. 4(b), the region of interest is only from  $t = 0.1$  to  $t = 1$ , as the final very slow coarsening stage is achieved sooner. A larger difference between the  $N = 97$  grid compared to the others is seen. There is little qualitative difference in the growth rates using grid sizes larger than  $N = 129$ , and thus that is the size chosen for the further analysis.

## C. Characteristic Length and Energy Evolution

In this section sample evolution curves for the characteristic length, Eq. (26), and the total energy of the system, Eq. (6), are examined over time for the CH and CHC systems, assuming both constant and variable mobility. To explore the CHC systems, 3 simulation results for each mobility case is shown. These will then be compared to a single CH simulation. As was mentioned earlier, the noise intensity level for the results in this section is  $\sigma = 10^{-5}$ .

The energy, Fig. 5, and characteristic length, Fig. 6, are shown over time for the single CH simulation and three representative CHC simulations. During the initial stage when the system is in a homogeneous state, the total energy is large and remains constant for both the CH and CHC systems. After some time the initial state segregates into many, small

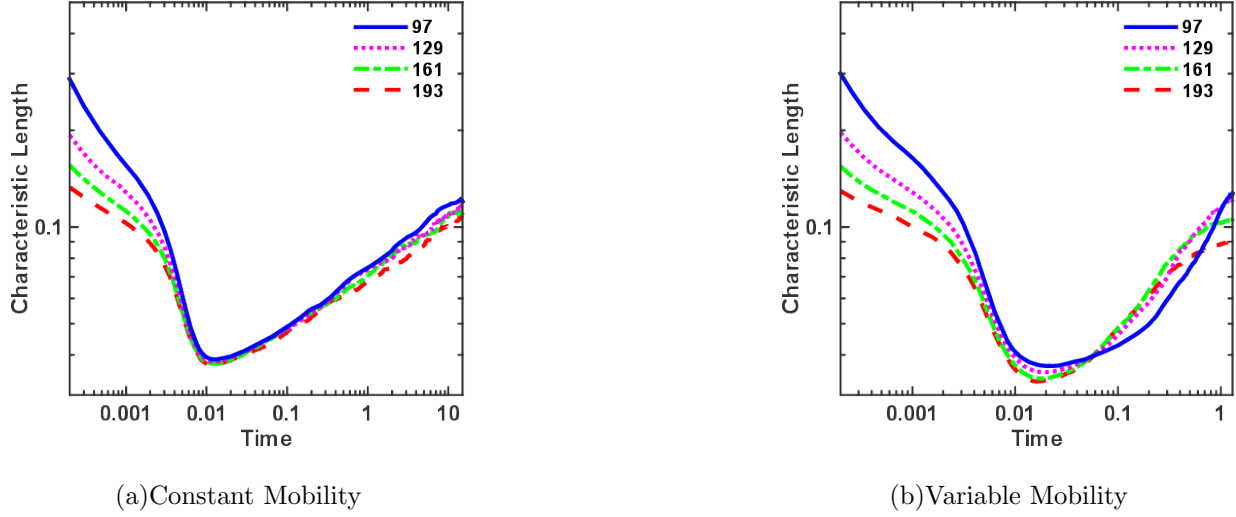
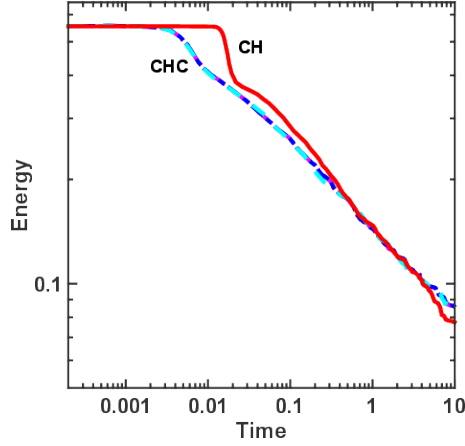


FIG. 4: The characteristic length over time using the Cahn-Hilliard-Cook model on a sphere with constant and variable mobilities for various grid sizes.

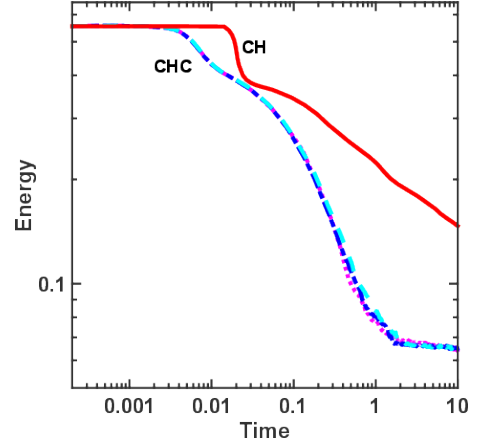
domains, see Fig. 3 for an example. During this rapid phase segregation regime both the CH and CHC simulations see an overall decrease in the characteristic length, eventually reaching a minimum length, while a rapid decrease in the overall energy occurs. In both mobility cases, the CHC model begins the segregation process earlier, as is evident from the earlier decrease of the energy. It is also interesting to note that the CH system has a brief increase in the characteristic length for both constant and variable mobility. This can be attributed to the CH system remaining near the well-mixed initial condition longer than the CHC system. Instead of quickly segregating to well-defined domains, the CH simulations have many, small amplitude fluctuations. This results in a relatively small value of  $L(t)$ , which quickly increases as the domains form.

After this rapid phase segregation, the system undergoes a steady and much slower coarsening process. For the constant mobility case, Figs. 5(a) and 6(a), it is clear that the growth rate for the CHC system is below that of the CH system. At a time of  $t = 10$  the energy of the system is higher and the characteristic length is smaller for the CHC system as compared to the CH system. Thus, while noise promotes the early start of the coarsening process when constant mobility is assumed, it inhibits the process during the slower, second coarsening regime.

The assumption of variable mobility dramatically changes the influence of the noise, see, Figs. 5(b) and 6(b). While the CHC system begins to segregate earlier than the CH system,

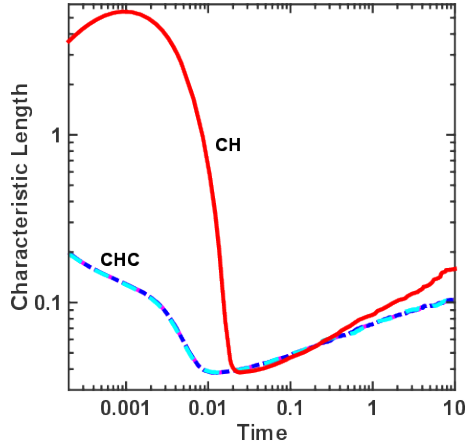


(a) Constant Mobility

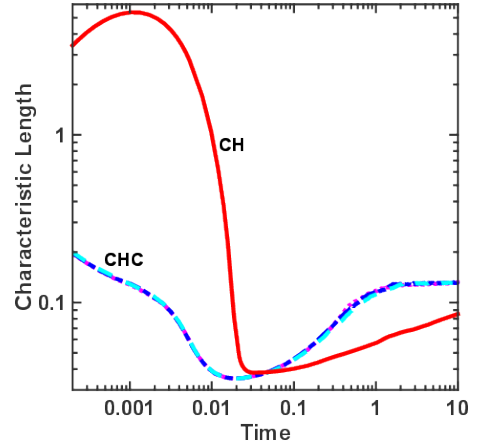


(b) Variable Mobility

FIG. 5: The change of total energy in the Cahn-Hilliard model along with the three sample runs of a Cahn-Hilliard-Cook model for constant and variable mobilities.



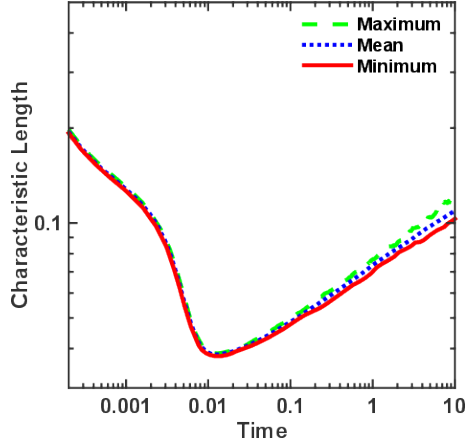
(a) Constant Mobility



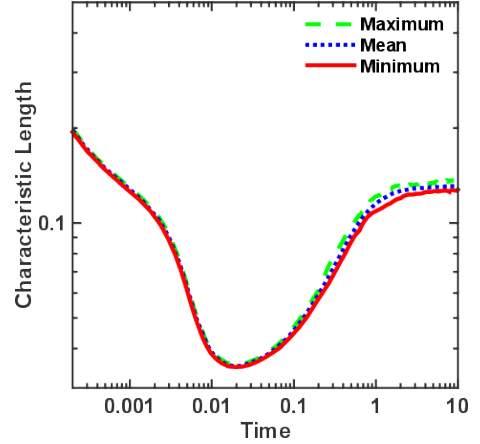
(b) Variable Mobility

FIG. 6: The characteristic length over time for the Cahn-Hilliard model along with three sample runs of the Cahn-Hilliard-Cook model for constant and variable mobilities.

similar to the constant mobility case, the rate of change of CHC with variable mobility is much higher than CH with variable mobility. It is suspected that the different scalings of the noise magnitude with respect to the mobility is the cause of this behavior. This will be further explored in Sec. IV D.



(a) Constant Mobility



(b) Variable Mobility

FIG. 7: The minimum, maximum, and mean characteristic lengths for the Cahn-Hilliard-Cook system for the 64 realizations using constant and variable mobilities each.

#### D. Discussion and Analysis

To further explore the CH and CHC systems, a total of 64 realizations (simulations) per noise level and mobility type have been performed. For the CHC system with  $\sigma = 10^{-5}$  the minimum, maximum, and average characteristic lengths for each time step have been determined from the 64 realizations, as shown in Fig. 7. Due to the cumulative effects of the noise during the course of the simulation, the spread of the characteristic length increases as time progresses.

After the initial segregation phase, it is expected that the characteristic length grows at a particular growth rate,  $\bar{R}(t) \propto t^\alpha$ , where  $\alpha$  is the growth rate. For the constant CH and CHC with constant mobility, in addition to the variable mobility CHC model, this region extends from approximately a time of  $t = 0.1$  to  $t = 10$ . Due to the faster dynamics of the variable mobility CHC model, this region exists approximately from  $t = 0.1$  to  $t = 0.8$ . After these times the system enters the long-term, slow growth phase. To determine the growth rate a linear fit is made to the appropriate region. The slope of this fit is taken to be the growth rate parameter  $\alpha$ . The complete results for the mean, standard deviation, and coefficient of variation for all considered systems is presented in Table I.

For the CH system, the growth rate for constant mobility was determined to be  $\bar{\alpha} = 0.2814$ , which differs from the theoretical growth rate of  $\alpha = 1/3$  for flat surfaces [74, 75].

TABLE I: Statistics on the growth rate for Cahn-Hilliard and Cahn-Hilliard-Cook model with constant and variable mobilities.

Model	Mobility	Noise	Mean	Standard Deviation	Coefficient of Variation
CH	1	–	0.2814	0.0215	0.0764
	$f(1 - f)$	–	0.1759	0.0062	0.0352
CHC	1	$10^{-9}$	0.2825	0.0197	0.0697
		$10^{-7}$	0.2672	0.0241	0.0902
		$10^{-5}$	0.1760	0.0134	0.0761
	$f(1 - f)$	$10^{-9}$	0.1765	0.0092	0.0521
		$10^{-7}$	0.3719	0.0148	0.0398
		$10^{-5}$	0.4278	0.0154	0.0360

This deviation from the theory indicates the underlying geometry does have an impact on the rate at which phase segregation occurs. In this case, the curvature of the sphere has played a role in retarding the rate of coarsening. When a degenerate mobility is used, this growth rate decreases to a value of  $\bar{\alpha} = 0.1759$ . As mentioned earlier, this decrease should be expected as the evolution process is now limited to only occur near the interface.

The CHC system is explored by not only varying the mobility type, but also the intensity of the noise,  $\sigma$ . First consider the constant mobility case. Using a noise intensity of  $\sigma = 10^{-5}$ , the average growth rate decreased to a value of  $\bar{\alpha} = 0.1760$ . As the noise intensity decreases, the mean approaches the that of the CH system, with values of  $\bar{\alpha} = 0.2672$  for  $\sigma = 10^{-7}$  and  $\bar{\alpha} = 0.2825$  for  $\sigma = 10^{-9}$ . This trend of recovering the Cahn-Hilliard system as the noise intensity is lowered has been also observed in the past [19].

When variable mobility is employed the mean growth rate of for a Cahn-Hilliard-Cook model increases to  $\bar{\alpha} = 0.4278$  when  $\sigma = 10^{-5}$ . As the noise intensity level decreases, the growth rate also decreases, with  $\bar{\alpha} = 0.3719$  for  $\sigma = 10^{-7}$  and  $\bar{\alpha} = 0.1765$  for  $\sigma = 10^{-9}$ . As with the constant mobility case, this growth rate approaches the Cahn-Hilliard value.

The fact that the growth rate increases for CHC and variable mobility is quite surprising.

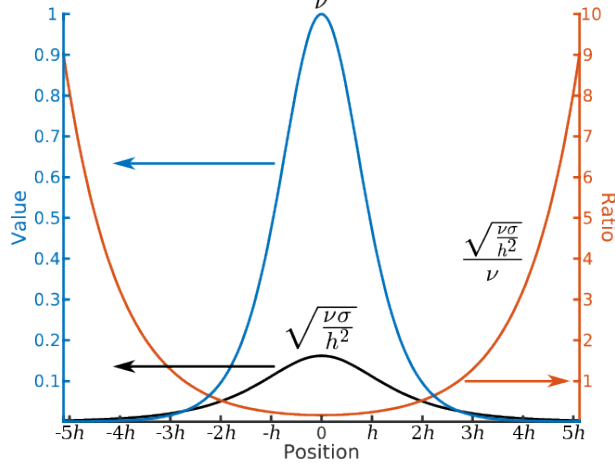


FIG. 8: The mobility ( $\nu = 4f(1 - f)$ ) and noise magnitude ( $\sqrt{\nu\sigma}/h^2$ ) where  $\sigma = 10^{-5}$  and  $h = 2.5/128$  for an equilibrium 1D profile, Eq. (27). The ratio of the noise magnitude to mobility is also provided.

One possible explanation can be obtained by comparing two contributions to  $\partial f/\partial t$ : the diffusive contribution  $\nu\Delta_s^2 f$  and the conserved random force  $\xi$ . The diffusive contribution will tend to smooth out any oscillations which occur while the random force will push the system away from an equilibrium configuration.

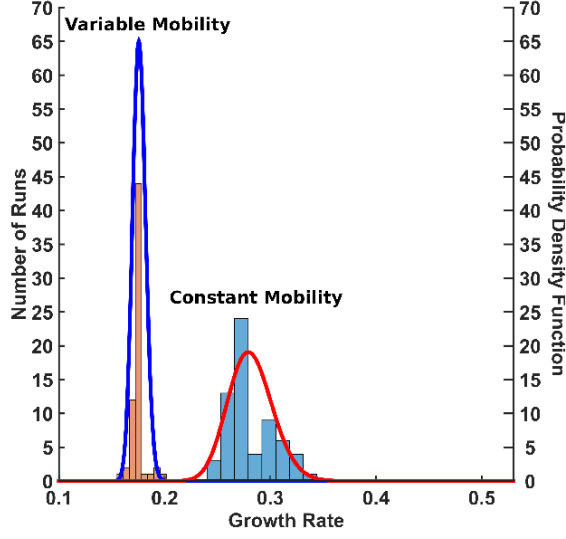
Consider a simple, 1D equilibrium phase field profile, which is given by [76]

$$f_{eq}(x) = \frac{1}{2} \left[ \tanh\left(\frac{x}{Cn\sqrt{2}}\right) + 1 \right]. \quad (27)$$

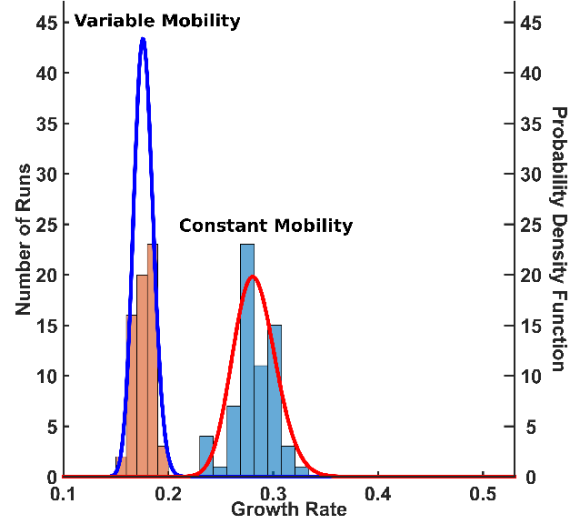
The diffusive contribution scales as the mobility,  $\nu$ , while at the discrete level the noise will scale as  $\sqrt{\nu\sigma}/h^2$ , Eq. (23). As an example use  $Cn = 0.015$  with  $\sigma = 10^{-5}$  and  $h = 2.5/128$ . The value of the mobility and of the noise scaling is presented in Fig. 8. The ratio between the noise scaling and the mobility is also shown in this figure.

Both the mobility and noise magnitude decrease quickly away from  $x = 0$ , with the mobility decreasing at a faster rate than the noise magnitude. This becomes apparent when the ratio is considered. In regions away from  $x = 0$  the influence of noise becomes more larger than the diffusive term. It is suspected that the larger influence of noise in regions away from the interface drive the system to coarsen faster than the other cases. This behavior also explains the oscillations (faint white patches) observed in the well-segregated regions in Fig. 3, as the influence of the noise is relatively large, compared to the diffusive terms.

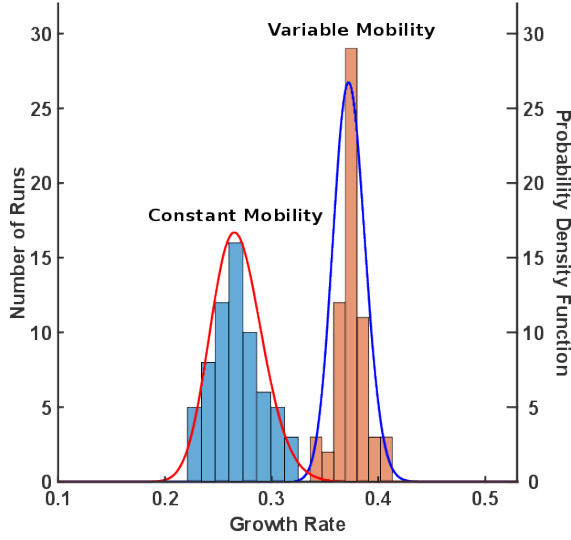
The complete CH and CHC results for various noise intensity levels can be seen in the



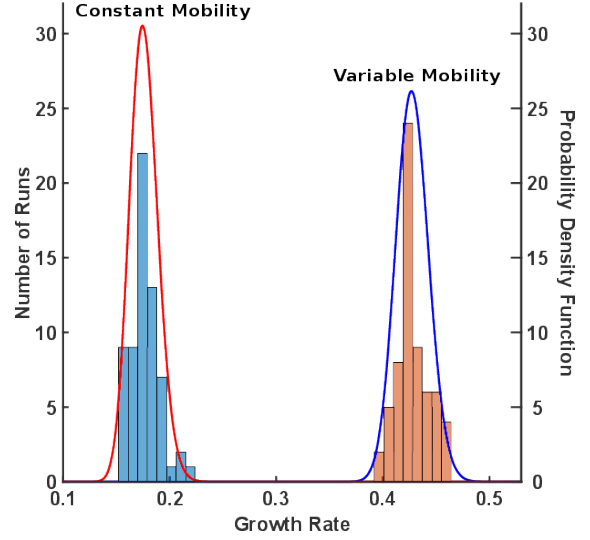
(a)CH



(b)CHC:  $\sigma = 10^{-9}$



(c)CHC:  $\sigma = 10^{-7}$



(d)CHC:  $\sigma = 10^{-5}$

FIG. 9: Histograms for the growth rate of the characteristic length for CH and CHC systems using 64 realizations for constant and variable mobilities. A log-normal distribution function is fit on the results.

histograms shown in Fig. 9. Using this data a probability density function is fit and also shown on the histograms. As the growth rate can never be negative, only non-negative distributions were explored. The log-normal distribution gave a good qualitative fit and as the null hypothesis also passed the Kolmogorov-Smirnov test at 5% level of significance [77] for all situations, it is chosen to be an appropriate fit.



TABLE II: Parameter estimates for the log-normal distribution function that fits the histogram of the growth rate for the CH and CHC systems with constant and variable mobilities.

Model	Mobility	Noise	$\mu$	$\sigma_{pdf}$
CH	1	–	–1.2707	0.0748
	$f(1-f)$	–	–1.7384	0.0349
CHC	1	$10^{-9}$	–1.2664	0.0716
		$10^{-7}$	–1.3237	0.0902
		$10^{-5}$	–1.7339	0.0747
	$f(1-f)$	$10^{-9}$	–1.7358	0.0523
		$10^{-7}$	–0.9900	0.0402
		$10^{-5}$	–0.8498	0.0357

The probability density function of the log-normal distribution is given by

$$f(x|\mu, \sigma_{pdf}) = \frac{1}{x\sigma_{pdf}\sqrt{2\pi}} \exp\left(\frac{-(\ln x - \mu)^2}{2\sigma_{pdf}^2}\right) \quad \text{with} \quad x > 0, \quad (28)$$

where  $x$  is the data,  $\mu$  is the log mean, and  $\sigma_{pdf}$  is log standard deviation with the support  $-\infty < \mu < \infty$  and  $\sigma_{pdf} \geq 0$ . The log mean and the log standard deviation can be estimated from the probability density function. See Table II for the fitted parameters. It is noted as the noise intensity goes down the log mean value approaches the result for the Cahn-Hilliard system.

## V. DUMBBELL INTERFACE

In this section the phase segregation on a dumbbell is examined. The shape are two spheres connected by a cylinder. Each sphere has a radius of 0.75 and are centered at  $(-1.125, 0, 0)$  and  $(1.125, 0, 0)$  while the cylinder connecting the two sphere has a radius of 0.375. The average concentration is 0.3 while the initial random perturbation has a magnitude of 0.01. To focus on the influence of the underlying geometry, only the constant-mobility case is considered.

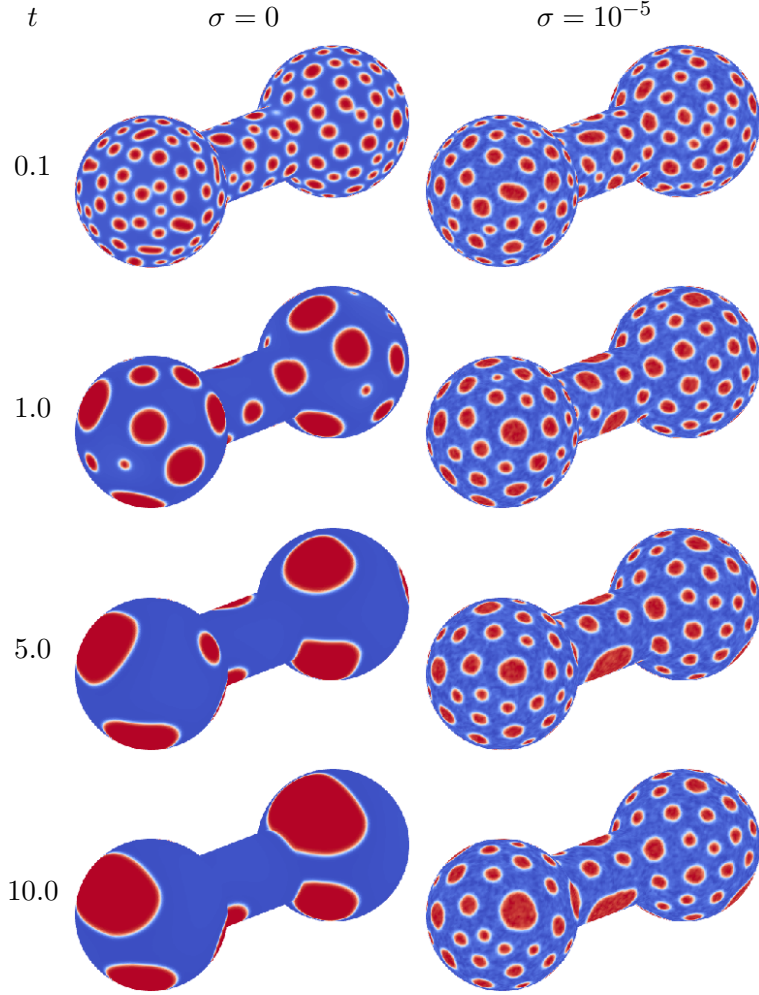
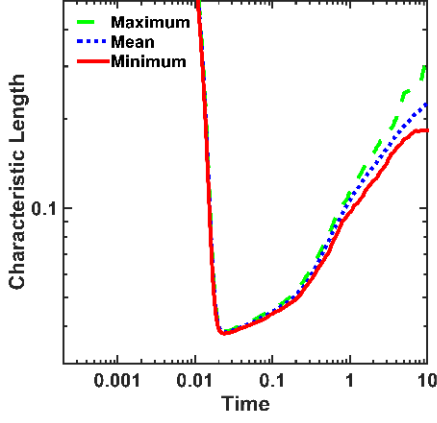


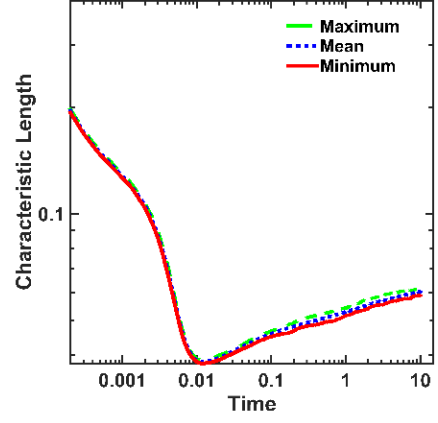
FIG. 10: Evolution for Cahn-Hilliard ( $\sigma = 0$ ) and Cahn-Hilliard-Cook ( $\sigma = 10^{-5}$ ) model with constant mobility on a dumbbell.

First consider the Cahn-Hilliard system, Fig. 10. As before, the initially well-mixed system quickly segregates into many, small domains. Over time, the domains begin to grow and coarsen, until a small number of large domains exist. Next consider the Cahn-Hilliard-Cook system with  $\sigma = 10^{-5}$ , again Fig. 10. As with the CH system, the well-mixed system quickly segregates into small domains. Unlike the CH case, the growth rate of the domains using the CHC model on the dumbbell is greatly reduced, as seen by the many, small domains at a time of  $t = 10$ . This indicates that the underlying geometry has a large influence on the coarsening process in the presence of noise.

As before, a statistical analysis of the growth rate is done for the Cahn-Hilliard and the Cahn-Hilliard-Cook model using  $\sigma = 10^{-5}$ , using 64 realizations for each model. The



(a)Cahn Hilliard Model



(b)Cahn Hilliard Cook Model

FIG. 11: The minimum, maximum, and mean characteristic lengths for the Cahn-Hilliard and Cahn-Hilliard-Cook system for the 64 realizations using constant mobility on a dumbbell.

TABLE III: Statistics on the growth rate for Cahn-Hilliard and Cahn-Hilliard-Cook model with constant mobility of a dumbbell

Model	Time	Noise	Mean	Standard Deviation	Coefficient of Variation
CH	0.02 - 0.2	—	0.1380	0.0073	0.0529
	1 - 10	—	0.3152	0.0607	0.1926
CHC	0.1-10	$10^{-5}$	0.0581	0.0050	0.0861

minimum, maximum, and average characteristic length for each time step is plotted in Fig. 11. As expected, the characteristic length for both the CH and CHC model increases over time, with the spread between the minimum growth rate and the maximum growth rate also increasing with time. Additionally, the mean, standard deviation, and coefficient of variation are shown in Table III while the corresponding histograms are shown in Fig. 12.

When considering the CH model, there are two growth rates apparent in the system. The first extends from  $t = 0.02$  to  $t = 0.2$ , while the second extends from  $t = 0.2$  onward. It is therefore appropriate to consider two growth rates, with  $\bar{\alpha} = 0.1380$  from  $t = 0.02$  to  $t = 0.2$  and  $\bar{\alpha} = 0.3152$  from  $t = 0.2$  onwards. When considering this latter regime, the standard

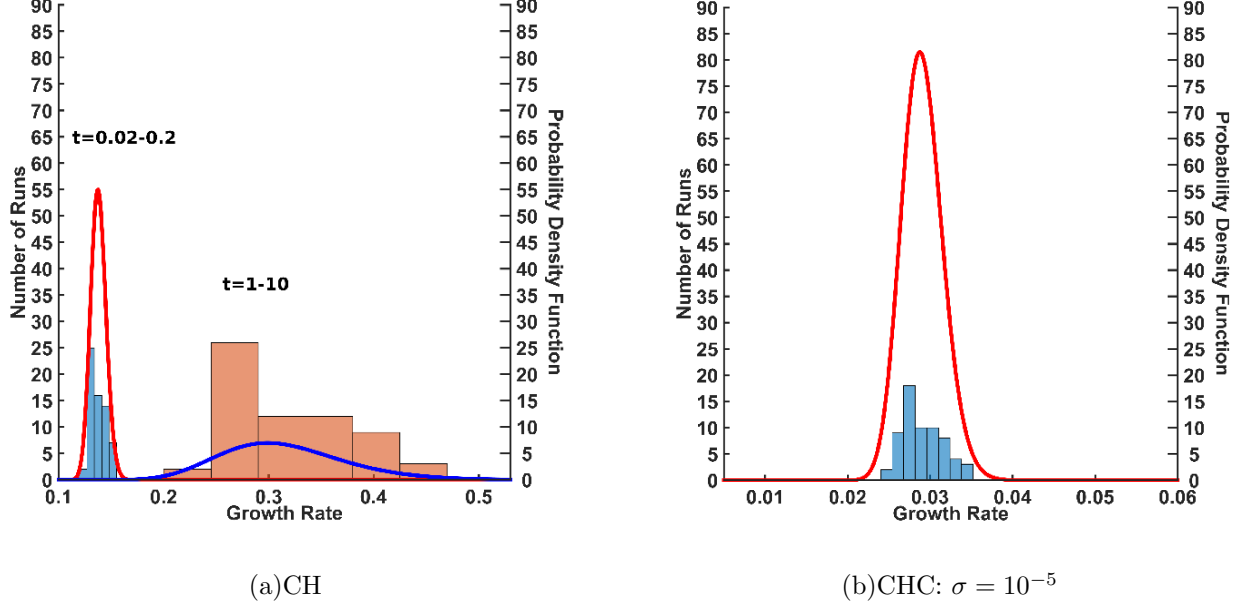


FIG. 12: Histograms for the growth rate of the characteristic length for CH and CHC systems using 64 realizations for constant mobility on a dumbbell. A log-normal distribution function is fit on the results.

deviation and coefficient of variation is quite large, as shown in Table III. It is suspected that the underlying interface plays a large role in the large variation in the growth rate at late time. To demonstrate this, consider two sample runs shown in Fig. 13. At a time of  $t = 0.5$ , both interfaces are well-covered by small domains, with the distance between domains similar. At a time of  $t = 10$ , the domains for Run I are predominantly on the two spheres, with no domain on the connecting cylinder. In Run II, there is a domain on the cylinder. The distance between domains plays a critical role in the coarsening process, with a larger distance corresponding to a lower growth rate. Unlike the spherical interface, the lack of full symmetry in the dumbbell shape results in a growth rate which depends on the initial condition, as that will determine where large domains will preferentially occur.

Now consider the Cahn-Hilliard-Cook system with noise intensity of  $10^{-5}$ . From the sample result in Fig. 10 and Table III, it is apparent that the growth rate is very small, with a value of  $\bar{\alpha} = 0.0581$  and a small standard deviation of 0.005. It is suspected that the larger curvatures present in the dumbbell shape, coupled with the large noise intensity, results in this decrease in the growth rate.

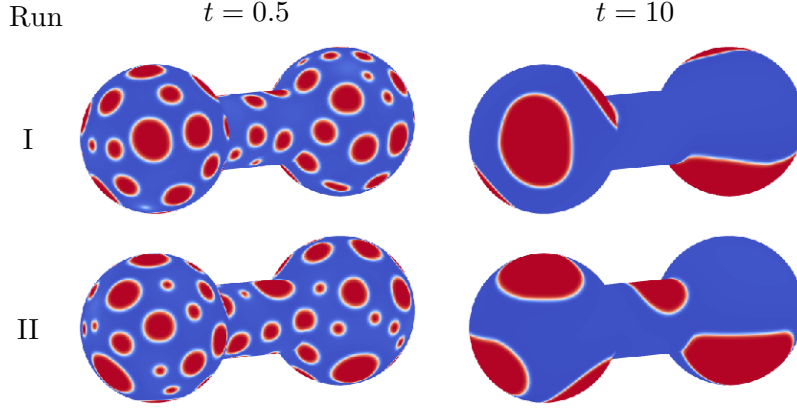


FIG. 13: Evolution for Cahn-Hilliard model with constant mobility on a dumbbell, for two realizations.

## VI. CONCLUSION

In this work the Cahn-Hilliard-Cook model is solved on smooth interfaces using a splitting method that converts the fourth-order partial differential equation into a two coupled second-order PDEs. The surface differential equations are solved using the Closet Point Method, using a level-set Jet scheme to describe the interface.

These results indicate that the underlying surface plays a large role in the segregation process, both in the presense and in the absence of thermal fluctuations/noise. When assuming constant surface mobility, the presense of noise slows the coarsening rate of domains, with the growth rate increasing with a decrease in the noise magnitude. Surprisingly, the presense of noise actually increases the growth rate when assuming a degenerate mobility. This is most likely due to the fact that the diffusive evolution contributions decay at a faster rate than the noise contributions as one moves away from the interface.

When examining a spherical interface in the absence of noise, the overall growth rate is slightly lower than that predicted for flat, two-dimensional surfaces. The inclusion of noise further decreases the observed growth rate. The use of a dumbbell shape, with a spatially varying curvature, further influences the evolution. Assuming no noise, two growth regimes were identified on the dumbbell, with the final growth rate highly dependent on the initial condition. Inclusion of noise for the dumbbell shape dramatically decreased the growth rate.

## Acknowledgments

This work has been supported by the National Science Foundation through the Division of Chemical, Bioengineering, Environmental, and Transport Systems Grant #1253739.

---

- [1] S. Takagi and Y. Matsumoto, Annual Review of Fluid Mechanics **43**, 615 (2011).
- [2] N. R. Morrow and G. Mason, Current Opinion in Colloid & Interface Science **6**, 321 (2001).
- [3] J. Goerke, Biochimica et Biophysica Acta (BBA)-Molecular Basis of Disease **1408**, 79 (1998).
- [4] S. L. Ceccio, Annual Review of Fluid Mechanics **42**, 183 (2010).
- [5] M. Laradji and P. S. Kumar, Physical Review Letters **93**, 198105 (2004).
- [6] A. S. Shaw, Nature Immunology **7**, 1139 (2006).
- [7] P. Peczak, G. S. Grest, and D. Levine, Physical Review E **48**, 4470 (1993).
- [8] P. Sens and S. Safran, The European Physical Journal E **1**, 237 (2000).
- [9] P. Tang, F. Qiu, H. Zhang, and Y. Yang, Physical Review E **72**, 016710 (2005).
- [10] J. W. Cahn and J. E. Hilliard, Journal Of Chemical Physics **28**, 258 (1958).
- [11] D. A. Cogswell, Ph.D. thesis, Massachusetts Institute of Technology (2010).
- [12] D. Jacqmin, AIAA paper pp. 96–0858 (1996).
- [13] E. K. Longmire, J. S. Lowengrub, and D. L. Gefroh, Urbana **51**, 61801 (1999).
- [14] C. M. Funkhouser, F. J. Solis, and K. Thornton, Journal Of Chemical Physics **140**, 144908 (2014).
- [15] S. M. Wise, J. S. Lowengrub, H. B. Frieboes, and V. Cristini, Journal of Theoretical Biology **253**, 524 (2008).
- [16] H. Cook, Acta Metallurgica **18**, 297 (1970), ISSN 0001-6160.
- [17] J. Langer, M. Bar-On, and H. D. Miller, Physical Review A **11**, 1417 (1975).
- [18] M. Grant, M. San Miguel, J. Vials, and J. Gunton, Physical Review B **31**, 3027 (1985).
- [19] T. Rogers, K. Elder, and R. C. Desai, Physical Review B **37**, 9638 (1988).
- [20] M. Ibanes, J. García-Ojalvo, R. Toral, and J. Sancho, The European Physical Journal B-Condensed Matter and Complex Systems **18**, 663 (2000).
- [21] J. García-Ojalvo, A. Lacasta, J. M. Sancho, and R. Toral, EPL (Europhysics Letters) **42**, 125 (1998).

- [22] X. Zheng, C. Yang, X.-C. Cai, and D. Keyes, *Journal of Computational Physics* **285**, 55 (2015).
- [23] J. Fan, M. Sammalkorpi, and M. Haataja, *Physical Review E* **81**, 011908 (2010).
- [24] A. Karma and W.-J. Rappel, *Physical Review E* **60**, 3614 (1999).
- [25] C. Shen, J. Simmons, and Y. Wang, *Acta materialia* **55**, 1457 (2007).
- [26] O. Wodo and B. Ganapathysubramanian, *Computational Materials Science* **55**, 113 (2012).
- [27] D. M. Saylor, C.-S. Kim, D. V. Patwardhan, and J. A. Warren, *Acta Biomaterialia* **3**, 851 (2007).
- [28] D. Furihata, *Numerische Mathematik* **87**, 675 (2001).
- [29] S. Choo and S. Chung, *Computers & Mathematics with Applications* **36**, 31 (1998).
- [30] C. M. Elliott, D. A. French, and F. Milner, *Numerische Mathematik* **54**, 575 (1989).
- [31] C. M. Elliott and D. A. French, *SIAM Journal on Numerical Analysis* **26**, 884 (1989).
- [32] S. Zhang and M. Wang, *Journal of Computational Physics* **229**, 7361 (2010).
- [33] L. Chen and J. Shen, *Computer Physics Communications* **108**, 147 (1998).
- [34] Y. He, Y. Liu, and T. Tang, *Applied Numerical Mathematics* **57**, 616 (2007).
- [35] A. H. de Vries, A. E. Mark, and S. J. Marrink, *Journal of the American Chemical Society* **126**, 4488 (2004).
- [36] W. Shinoda, R. DeVane, and M. L. Klein, *The Journal of Physical Chemistry B* **114**, 6836 (2010).
- [37] S. J. Marrink and A. E. Mark, *Journal of the American Chemical Society* **125**, 15233 (2003).
- [38] L. Bagatolli and P. S. Kumar, *Soft Matter* **5**, 3234 (2009).
- [39] D. Marenduzzo and E. Orlandini, *Soft Matter* **9**, 1178 (2013).
- [40] J. B. Greer, A. L. Bertozzi, and G. Sapiro, *Journal of Computational Physics* **216**, 216 (2006).
- [41] O. Wodo and B. Ganapathysubramanian, *Journal of Computational Physics* **230**, 6037 (2011).
- [42] J. Lowengrub, J. Xu, and A. Voigt, *Fluid Dyn. Mater. Proc* **3**, 1 (2007).
- [43] S. Li, J. Lowengrub, and A. Voigt, *Communications in Mathematica Sciences* **10**, 645 (2012).
- [44] D. Jeong and J. Kim, *The European Physical Journal E* **38**, 117 (2015).
- [45] J. W. Cahn, *Acta Metallurgica* **9**, 795 (1961).
- [46] A. Lacasta, A. Hernández-Machado, and J. M. Sancho, *Physical Review B* **48**, 9418 (1993).
- [47] S. Dai and Q. Du, *Journal of Computational Physics* **310**, 85 (2016).
- [48] H. Gómez, V. M. Calo, Y. Bazilevs, and T. J. Hughes, *Computer Methods in Applied Me-*

- chanics and Engineering **197**, 4333 (2008).
- [49] J. Lowengrub, A. Ratz, and A. Voigt, Physical Review E **79**, 031926 (2009).
  - [50] S. Delong, B. E. Griffith, E. Vanden-Eijnden, and A. Donev, Physical Review E **87**, 033302 (2013).
  - [51] B. Seibold, R. R. Rosales, and J.-C. Nave, Discrete & Continuous Dynamical Systems-Series B **17** (2012).
  - [52] G. Velmurugan, E. M. Kolahdouz, and D. Salac, Computer Methods in Applied Mechanics and Engineering **310**, 233 (2016).
  - [53] S. Osher and J. A. Sethian, Journal of Computational Physics **79**, 12 (1988).
  - [54] C. S. Hogue, B. T. Murray, and J. A. Sethian, Journal of Mathematical Biology **53**, 86 (2006).
  - [55] J. A. Sethian and J. Straint, Journal of Computational Physics **98**, 231 (1992).
  - [56] D. Salac and W. Lu, Computational Materials Science **39**, 849 (2007).
  - [57] D. Adalsteinsson and J. Sethian, Journal of Computational Physics **138**, 193 (1997).
  - [58] S. Osher and R. P. Fedkiw, Journal of Computational physics **169**, 463 (2001).
  - [59] J. Sethian and P. Smereka, Annual Review of Fluid Mechanics **35**, 341 (2003).
  - [60] B. Fornberg, Mathematics Of Computation **51**, 699 (1988), ISSN 0025-5718.
  - [61] S. J. Ruuth and B. Merriman, Journal of Computational Physics **227**, 1943 (2008).
  - [62] C. B. Macdonald and S. J. Ruuth, SIAM Journal on Scientific Computing **31**, 4330 (2009).
  - [63] Y. Chen and C. Macdonald, SIAM Journal on Scientific Computing **37**, A134 (2015).
  - [64] S. Balay, F. Brown, K. Buschelman, W. Gropp, D. Kaushik, M. Knepley, L. McInnes, B. Smith, and H. Zhang, *PETSc Web page* (2012), <http://www.mcs.anl.gov/petsc>.
  - [65] S. Balay, F. Brown, K. Buschelman, V. Eijkhout, W. Gropp, D. Kaushik, M. Knepley, L. McInnes, B. Smith, and H. Zhang, Tech. Rep. ANL-95/11 - Revision 3.3, Argonne National Laboratory (2012).
  - [66] S. Balay, W. Gropp, L. McInnes, and B. Smith, in *Modern Software Tools in Scientific Computing*, edited by E. Arge, A. M. Bruaset, and H. P. Langtangen (Birkhäuser Press, 1997), pp. 163–202.
  - [67] M. Gee, C. Siefert, J. Hu, R. Tuminaro, and M. Sala, Tech. Rep. SAND2006-2649, Sandia National Laboratories (2006).
  - [68] K. H. Lloyd, Tech. Rep., DTIC Document (1982).
  - [69] D. Enright, R. Fedkiw, J. Ferziger, and I. Mitchell, Journal of Computational Physics **183**,



- 83 (2002).
- [70] M. Sussman, E. Fatemi, P. Smereka, and S. Osher, *Computers & Fluids* **27**, 663 (1998).
  - [71] M. Sussman and E. G. Puckett, *Journal of Computational Physics* **162**, 301 (2000).
  - [72] J.-J. Xu, Z. Li, J. Lowengrub, and H. Zhao, *Journal of Computational Physics* **212**, 590 (2006).
  - [73] P. Gera and D. Salac, *Applied Mathematics Letters* (2017), Accepted.
  - [74] M. Kahlweit, *Advances in Colloid and Interface Science* **5**, 1 (1975), ISSN 0001-8686.
  - [75] I. M. Lifshitz and V. V. Slyozov, *Journal of Physics and Chemistry of Solids* **19**, 35 (1961).
  - [76] D. Lee, J.-Y. Huh, D. Jeong, J. Shin, A. Yun, and J. Kim, *Computational Materials Science* **81**, 216 (2014), ISSN 0927-0256.
  - [77] I. Chakravati, R. Laha, and J. Roy, *Handbook of Methods of Applied Statistics, Volume I* (1967).